Research Article Vol. 16, No. 8 / 1 Aug 2025 / Biomedical Optics Express 3139
Biomedical Optics EXPRESS

Enhanced supercritical angle localization microscopy through point spread function modeling

SAJJAD A. KHAN,[1,2] KEITH A. LIDKE,[1] AND SHENG LIU[1,*]

[1]Department of Physics and Astronomy, University of New Mexico, Albuquerque, New Mexico, USA
[2]Nanoscience and Microsystems Engineering, University of New Mexico, Albuquerque, New Mexico, USA
*shengliu@unm.edu

Abstract: Single-molecule localization microscopy (SMLM) enables precise spatial localization of single molecules in cellular structures. A phenomenon called supercritical angle fluorescence (SAF) is utilized in SMLM (SAF-SMLM) to estimate the axial positions of single fluorophores. It is based on the fact that SAF intensity is highly sensitive to the fluorophore-coverslip distance. Conventional SAF-SMLM methods typically involve splitting the fluorescence emission into supercritical and undercritical components, which requires a complicated two-channel system and can lead to reduced light efficiency. In this work, we introduce a simplified approach to traditional SAF-SMLM by directly detecting all fluorescence into a single channel. Through simulations, we found that by accurately modeling the point spread function (PSF) with SAF, a single-channel system achieves better localization precision than two-channel-based SAF-SMLM systems. Furthermore, we developed a stage-tilt correction algorithm, incorporating stage tilt in the PSF model, to improve axial precision over the entire field of view. We applied our method experimentally by imaging F-actin filaments in HeLa cells. We demonstrate that our method efficiently exploits the information from SAF and achieves enhanced axial localization precision and accuracy compared to traditional SMLM localization methods for single-channel systems.

© 2025 Optica Publishing Group under the terms of the Optica Open Access Publishing Agreement

1. Introduction

Single-molecule localization microscopy (SMLM) [1–3] is one of the super-resolution microscopy techniques that circumvents the diffraction-limited resolution of fluorescence microscopy. For 2D localization, the lateral positions can be estimated by modeling the emission pattern of a single emitter, the point spread function (PSF), with a 2D Gaussian. For 3D localization, many techniques have been developed to encode the emitter's axial position in the shape of the PSF. These techniques include astigmatism imaging [4], multi-plane imaging [5,6], 4Pi interferometric detection [7], and PSF engineering such as double-helix PSF [8,9], TetraPod [10] or saddle-point PSF [11].

Additionally, some techniques explored the benefit of supercritical angle fluorescence (SAF) on axial localization. SAF comes from the non-propagating evanescent wave of the dipole radiation from a single fluorophore. When a fluorophore is close to the sample/coverslip interface, the evanescent wave couples through the interface, becoming a propagating wave inside the immersion medium and propagating at an angle above the critical angle [Fig. 1(a,b)]. SAF only occurs when the refractive index of the sample medium is less than that of the immersion medium and the objective's numerical aperture (NA) is larger than the refractive index of the sample medium. This is often the case when imaging an aqueous sample with a high NA objective. The magnitude of SAF decays exponentially with the emitter's distance to the coverslip. This feature has been applied to SMLM to infer the emitter's axial position. One method, termed direct optical nanoscopy with axially localized detection (DONALD) [12] or supercritical angle localization microscopy (SALM) [13], splits the emission equally into two channels, with one

#563592 https://doi.org/10.1364/BOE.563592
Journal © 2025 Received 3 Apr 2025; revised 27 Jun 2025; accepted 27 Jun 2025; published 10 Jul 2025

Biomedical Optics EXPRESS

channel detecting both the SAF and undercritical fluorescence (UAF) and another channel detecting only the UAF. The photon ratio between the SAF and UAF can be calculated from the raw data and subsequently used for axial localization. However, this method loses half of the SAF. Another method, direct supercritical angle localization microscopy (dSALM) [14], overcame this problem by directly splitting the SAF and UAF into two channels.

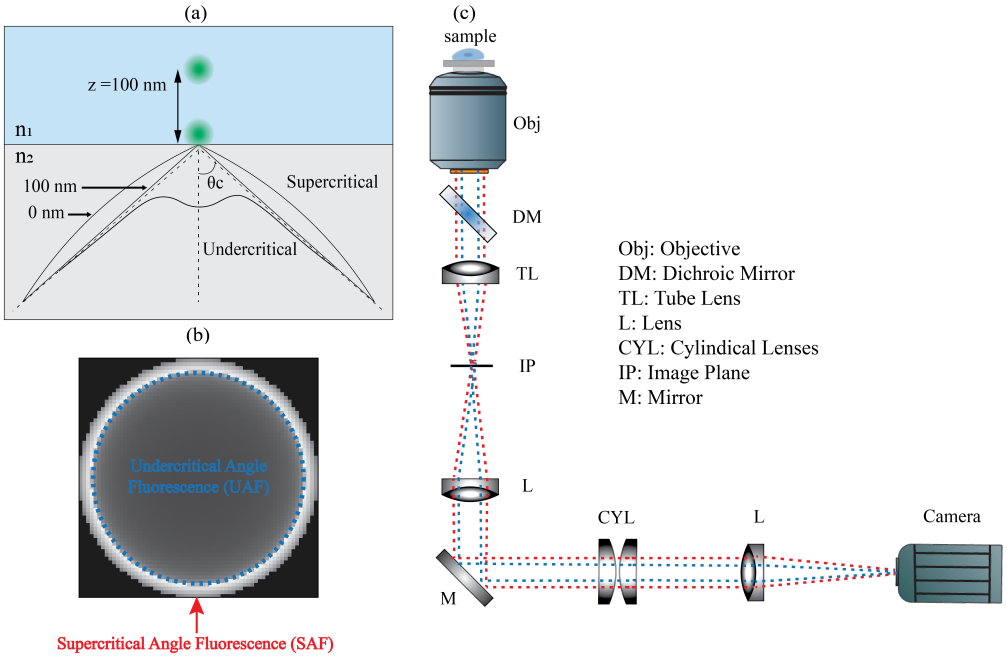

Fig. 1. **a:** Supercritical angle fluorescence (SAF) occurs when a fluorophore is in close vicinity to a glass-water interface, causing near-field fluorescence to be collected in supercritical angles. **b:** Pupil image of a microscope with SAF. The dotted ring separates the SAF and UAF components. **c:** Schematic of the single-channel system used in this work. The dotted lines show the beam path of SAF (red) and UAF (blue).

The exponential decay of SAF limits the axial localization to a small z range near the coverslip. Both DONALD and dSALM [12,14,15] can be modified by adding a cylindrical lens in the UAF channel to improve the axial localization precision over a larger axial range. This requires PSF modeling of the UAF channel. Furthermore, a recent study theoretically demonstrated that incorporating the PSF information from both channels of SALM/DONALD improves the axial precision over a larger z range [16]. The same work also proposed an off-focus imaging technique that uses the PSF information from defocused images of a single-channel system to achieve better axial precision compared to SALM/DONALD methods. A follow-up study compared commonly used 3D SMLM techniques in the presence of SAF and concluded that bi-plane imaging performs the best in exploiting the information from SAF [17]. Those works raise the importance of PSF modeling in SAF-based 3D SMLM techniques. Traditional methods based on separating UAF and SAF, DONALD/SALM/dSALM, might not be optimal for utilizing SAF-induced information. In the following text, we use SAF-SMLM as a general term referring to 3D SMLM techniques that utilize SAF-induced information.

Here we compared the theoretical localization precisions of three SAF-SMLM techniques: 1) a single-channel system with PSF modeling that incorporates SAF, termed single-channel SAF-PSF modeling [Fig. 1(c)], 2) dSALM with PSF modeling, and 3) dSALM with photometry that uses the exponential decay feature of SAF. We demonstrated that single-channel SAF-PSF

Biomedical Optics EXPRESS

modeling outperforms dSALM-based methods. And adding astigmatism substantially improves the axial precision for PSF-modeling based methods. Although biplane imaging outperforms astigmatism imaging, it complicates the imaging system [17]. In this work, we focused on astigmatism imaging with SAF. Traditional SALM techniques extract the PSF models from bead data, which does not directly represent the emission patterns from single fluorophores. To obtain an accurate PSF model, we applied an *in-situ* PSF-modeling method to extract the PSF model directly from single-molecule data [18]. Furthermore, we demonstrate that in the presence of the SAF, PSF models are more sensitive to the coverslip tilt. An overall sample-stage tilt of 100-300 nm across a field of view (FOV) of 30×30 μm^2 is often inevitable in most imaging systems. However, this amount of stage tilt is large enough to induce variation in the PSF models at different lateral positions. Here, we developed a stage-tilt correction algorithm to incorporate the stage tilt in the PSF model to improve the axial precision over the full FOV. We demonstrated the performance of our developed method by imaging actin filaments near the coverslip.

2. Theory

2.1. Vectorial PSF model with supercritical angle fluorescence

A microscope image is created by convolving the structure of the sample with the PSF. Precise modeling of the PSF is crucial for accurate localization of point emitters in SMLM [19]. In fluorescent imaging, point emitters are single fluorophores that can be modeled as dipole emitters, whose PSFs are calculated from vectorial diffraction theory. In many fluorescent-labeled samples, we can consider the fluorophore as a freely rotating dipole, where the dipole rotation is much faster than the fluorescent lifetime. The PSF model of a freely rotating dipole at position (x_i, y_i, z_i) and sampled at the image coordinate (x, y) is given by [18,20],

$$PSF(x - x_i, y - y_i, z_i) = \sum_{\substack{m=x,y \\ n=p_x,p_y,p_z}} |\mathcal{F}[h(k_x, k_y) w_{mn} e^{i2\pi(k_x x_i + k_y y_i + k_z z_i)}]|^2, \tag{1}$$

where $\mathcal{F}$ denotes the Fourier transform, and $h(k_x, k_y)$ is the complex pupil function. k_x, k_y and k_z are the x, y and z components of the wave vector with its magnitude $k = n_{\text{imm}}/\lambda$, where n_{imm} is the refractive index of the immersion medium. Here p_x, p_y and p_z are the Cartesian components of the dipole moment, and w_{mn} is the electric field at the pupil plane in m polarization, generated from the n component of the dipole moment [18]. The pupil function of most imaging systems has a circular boundary, and its cutoff frequency is defined by n_a/λ, with n_a being the NA of the objective. The complex pupil function is typically expressed in terms of its magnitude $A(k_x, k_y)$ and its phase $\Phi(k_x, k_y)$,

$$h(k_x, k_y) = A(k_x, k_y) e^{i\Phi(k_x, k_y)}, \tag{2}$$

We can express the magnitude (A) and phase (Φ) components of the pupil function in the basis of Zernike polynomials Z_p as,

$$A = \sum_p C_{A,p} Z_p, \quad \Phi = \sum_p C_{\Phi,p} Z_p. \tag{3}$$

The coefficients, $C_{A,p}$ and $C_{\Phi,p}$, can be extracted from *in-situ* PSF-modeling (see section 3.1). When using an oil immersion objective, the mismatch between the refractive indices of the sample medium and the immersion oil leads to depth-dependent aberration [21,22], termed index mismatch aberration (IMM). Additionally, for high NA objectives and when emitters are close to the coverslip, the evanescent wave from near-field dipole radiation can penetrate the coverslip and propagate at an angle above the critical angle, producing SAF. SAF decreases as emitters

Biomedical Optics EXPRESS

move away from the coverslip. Incorporating both IMM and SAF into the vectorial PSF model, we rewrite Eq. (1) as [18],

$$PSF(x-x_i, y-y_i, z_i, z_s) = \sum_{\substack{m=x,y \\ n=p_x,p_y,p_z}} |\mathcal{F}[h(k_x,k_y)T_a w_{mn} e^{i2\pi(k_x x_i + k_y y_i + k_{\mathrm{zmed}} z_i - k_{\mathrm{zimm}} z_s)}]|^2, \quad (4)$$

where k_{zmed} and k_{zimm} represent the z components of the wave vectors in the sample and immersion mediums, respectively, and can be calculated from

$$k_{\mathrm{zmed}} = \sqrt{\frac{n_{\mathrm{med}}^2}{\lambda^2} - \frac{n_{\mathrm{imm}}^2}{\lambda^2}\sin\theta_{\mathrm{imm}}^2}, \quad (5)$$

$$k_{\mathrm{zimm}} = \frac{n_{\mathrm{imm}}}{\lambda}\cos\theta_{\mathrm{imm}}. \quad (6)$$

Here, n_{med} and n_{imm} are the refractive indices of the sample and immersion mediums, respectively. The apodization term $T_a = \sqrt{\cos\theta_{\mathrm{imm}}}/\cos\theta_{\mathrm{med}}$ arises from the conversion of a spherical wavefront to a plane wavefront after transmitting through the objective [18]. The angles θ_{imm} and θ_{med} indicate the propagation angles of the fluorescence emission in the immersion medium and the sample medium, respectively. When θ_{imm} is greater than the critical angle, k_{zmed} becomes imaginary $k_{\mathrm{zmed}} = i\alpha$, resulting in an exponential decay $e^{-\alpha z}$ along the z direction, subsequently leading to a decrease of SAF. The variable z_i is the emitter's axial position relative to the coverslip. As we assume no emitter is below the coverslip, we have $z_i \geq 0$ for all emitters. And z_s defines the stage position relative to the nominal focal position, which is defined as the physical stage position when the coverslip is in focus. Therefore, we have $z_s = 0$ when the stage is at the nominal focal position, and $z_s>0$ when the emitter above the coverslip is in focus. When $z_s<0$, all emitters will be out-of-focus. Therefore, in practice, we always set z_s to a positive value. When an emitter is away from the coverslip, which is $z_i>0$, the term $2\pi(k_{\mathrm{zmed}} z_i - k_{\mathrm{zimm}} z_s)$ will induce IMM.

2.2. Calculation of Cramér-Rao lower bound (CRLB)

2.2.1. Single-channel system

The Cramér-Rao lower bound (CRLB) defines the lowest estimation variance of a parameter θ_i [23–25],

$$\sigma_{\theta_i}^2 \geq \left[I^{-1}\right]_{ii}, \quad (7)$$

where I is the Fisher information matrix, σ denotes the estimation precision, and in the following text, we use σ to denote $\sqrt{CRLB}$. The Fisher information matrix is defined by,

$$I_{ij} = \mathrm{E}\left[\frac{\partial \ln(L)}{\partial\theta_i}\frac{\partial \ln(L)}{\partial\theta_j}\right], \quad (8)$$

where E denotes the expectation and L is the likelihood function between the model and the data. We assume that the pixel values in the data are independent between pixels and follow the Poisson distribution. Then for a single-channel system, the Fisher information matrix can be calculated from,

$$I_{ij} = \sum_q \frac{1}{\mu_q}\frac{\partial\mu_q}{\partial\theta_i}\frac{\partial\mu_q}{\partial\theta_j}, \quad (9)$$

where μ_q is the model evaluated at the qth pixel. Given the total photon s and the background photon per pixel b, the model of a single emitter can be calculated from,

$$\mu(x,y,z,s,b) = s\cdot\mu_0(x,y,z) + b, \quad (10)$$

where μ_0 is the PSF model of a single emitter located at position (x,y,z), given by Eq. (4). In this case, the estimation parameters are $\theta = \{x,y,z,s,b\}$.

Biomedical Optics EXPRESS

2.2.2. Two-channel system

For a two-channel system, such as splitting the SAF and UAF into two channels, the Fisher information matrix can be calculated from [21],

$$I_{ij} = \sum_q \frac{1}{\mu_{\mathrm{sa},q}} \frac{\partial \mu_{\mathrm{sa},q}}{\partial \theta_i} \frac{\partial \mu_{\mathrm{sa},q}}{\partial \theta_j} + \sum_q \frac{1}{\mu_{\mathrm{ua},q}} \frac{\partial \mu_{\mathrm{ua},q}}{\partial \theta_i} \frac{\partial \mu_{\mathrm{ua},q}}{\partial \theta_j}, \tag{11}$$

where μ_{sa} and μ_{ua} are the models for the SAF and UAF parts of a single emitter,

$$\mu_{\mathrm{sa}} = s \cdot \mu_{0,\mathrm{sa}}(x, y, z) + b_{\mathrm{sa}}, \tag{12}$$

$$\mu_{\mathrm{ua}} = s \cdot \mu_{0,\mathrm{ua}}(x, y, z) + b_{\mathrm{ua}}. \tag{13}$$

$\mu_{0,\mathrm{sa}}$ and $\mu_{0,\mathrm{ua}}$ represent the corresponding PSF models for SAF and UAF. Here we assume the background photons, b_{sa} and b_{ua}, are independent between the SAF and UAF channels. The estimation parameters are $\theta = \{x, y, z, s, b_{\mathrm{sa}}, b_{\mathrm{ua}}\}$.

2.2.3. Photometric system

In traditional SAF-SMLM techniques, the axial position of an emitter is estimated from the photon count ratio between the SAF and UAF channels. Here, we term this modeling method the photometric model. In the photometric model, P_{sa} and P_{ua} are the photon counts from the SAF and UAF parts of a single emitter,

$$P_{\mathrm{sa}} = sP_{0,\mathrm{sa}}(z) + Nb_{\mathrm{sa}}, \tag{14}$$

$$P_{\mathrm{ua}} = sP_{0,\mathrm{ua}}(z) + Nb_{\mathrm{ua}}, \tag{15}$$

where $P_{0,\mathrm{sa}}$ and $P_{0,\mathrm{ua}}$ are the sum of the corresponding PSF models for SAF and UAF. The information of the emitter's lateral position (x, y) is lost after the summation. $P_{0,\mathrm{sa}}$ and $P_{0,\mathrm{ua}}$ are scalars and are only dependent on z, so that P_{sa} and P_{ua} are also scalars. N is the number of pixels in the PSF model. In the photometric model, the estimation of b_{sa} and b_{ua} is strongly correlated with the estimation of s and z. To improve the estimation precision, b_{sa}, b_{ua} and s are often estimated independently using a two-channel PSF model [Eq. (12, 13)], and the photometric model is used only for estimating z. In this method, the errors of estimating b_{sa}, b_{ua} and s should be incorporated into the estimation precision of z. We applied the error propagation theory to calculate σ_z [14]. First, we rewrite Eq. (14) as

$$P_{\mathrm{sa}} - Nb_{\mathrm{sa}} = sP_{0,\mathrm{sa}}(z). \tag{16}$$

We then approximate the left side of the above equation as a linear function of z using the Taylor expansion,

$$P_{\mathrm{sa}} - Nb_{\mathrm{sa}} = sP_{0,\mathrm{sa}}(z_a) + s\frac{\partial P_{0,\mathrm{sa}}(z_a)}{\partial z}(z - z_a). \tag{17}$$

The above equation can be written as,

$$\frac{\partial P_{\mathrm{sa}}(z_a)}{\partial z}(z - z_a) = P_{\mathrm{sa}} - Nb_{\mathrm{sa}} - sP_{0,\mathrm{sa}}(z_a). \tag{18}$$

We define

$$f = \frac{\partial P_{\mathrm{sa}}(z_a)}{\partial z}(z - z_a). \tag{19}$$

Calculating the variance on both sides of above equation, we obtain,

$$\sigma_f^2 = \left[\frac{\partial P_{\mathrm{sa}}(z_a)}{\partial z}\right]^2 \sigma_z^2. \tag{20}$$

Biomedical Optics EXPRESS

The right side of Eq. (18) is a linear combination of variables, P_{sa}, b_{sa} and s. Based on error propagation theory, the estimation error of f is,

$$\sigma_f^2 = \sigma_{P_{\mathrm{sa}}}^2 + N^2\sigma_{b_{\mathrm{sa}}}^2 + P_{0,\mathrm{sa}}^2(z_a)\sigma_s^2. \tag{21}$$

As the measurement of P_{sa} follows a Poisson distribution, we have $\sigma_{P_{\mathrm{sa}}}^2 = P_{\mathrm{sa}}$. The variances $\sigma_{b_{\mathrm{sa}}}^2$ and σ_s^2 are given by the two-channel PSF model. We take the limit of $z_a \to z$, and obtain the estimation precision of z in the SAF channel from Eqs. (20,21),

$$\sigma_{z,\mathrm{sa}}^2 = \frac{\sigma_f^2}{\left[\frac{\partial P_{\mathrm{sa}}(z)}{\partial z}\right]^2} = \frac{P_{\mathrm{sa}} + N^2\sigma_{b_{\mathrm{sa}}}^2 + P_{0,\mathrm{sa}}^2(z)\sigma_s^2}{\left[\frac{\partial P_{\mathrm{sa}}(z)}{\partial z}\right]^2}. \tag{22}$$

Similarly, the estimation precision of z in the UAF channel is,

$$\sigma_{z,\mathrm{ua}}^2 = \frac{\sigma_f^2}{\left[\frac{\partial P_{\mathrm{ua}}(z)}{\partial z}\right]^2} = \frac{P_{\mathrm{ua}} + N^2\sigma_{b_{\mathrm{ua}}}^2 + P_{0,\mathrm{ua}}^2(z)\sigma_s^2}{\left[\frac{\partial P_{\mathrm{ua}}(z)}{\partial z}\right]^2}. \tag{23}$$

Combining Eqs. (22,23), we obtain the estimation precision of z based on the photometric model,

$$\frac{1}{\sigma_z^2} = \frac{1}{\sigma_{z,\mathrm{sa}}^2} + \frac{1}{\sigma_{z,\mathrm{ua}}^2}. \tag{24}$$

3. Correction of the stage tilt

In the presence of refractive index mismatching, the PSF model is dependent on the stage position [Eq. (4)]. To accurately estimate the emitter's position z_i, PSF-modeling based localization techniques require accurate estimation of the stage position. However, a slight tilt of the sample stage is often inevitable for most imaging systems. We found that an overall tilt of 100-300 nm across a FOV of 30×30 μm^2 is already significant to vary the PSF models, especially in the near-coverslip regime. In this section, we introduce a stage-tilt correction algorithm for accurately estimating emitters' axial positions near the coverslip using a single-channel system. We want to emphasize that stage-tilt correction is necessary only when considering SAF-PSF modeling. The photometric method does not require knowledge of the stage position, because the photon counts of the SAF and UAF channels are independent of the stage position. On the other hand, when imaging emitters far away from the coverslip, i.e., outside the detection range of SAF, the PSF model is no longer sensitive to a small stage tilt.

3.1. Extraction of the PSF model

We extract an *in-situ* PSF model directly from the raw blinking data of SMLM imaging. We utilize the inverse modeling concept from uiPSF to estimate the Zernike expanded pupil functions. Inverse modeling of PSF is an iterative approach in which the PSF model, e.g., Eq. (1), is first built from initial parameters, and is then compared to the experimental data to obtain their difference ('loss function'), followed by an optimization algorithm to adjust the model parameters to decrease the loss. This process is repeated until the convergence of the PSF model. *In-situ* PSF modeling involves four major steps: 1) select candidate emitters from raw SMLM data; 2) localize the emitters using an initial PSF model; 3) select a set of emitters with the lowest localization errors and covering the entire axial range; 4) estimate the PSF model from the selected emitters. This estimated PSF model is then used as the initial PSF model, and steps 2-4 are repeated two times.

Biomedical Optics EXPRESS

Figure 2(a) shows the extracted pupil function from *in-situ* PSF modeling. Figure 2(b) shows the retrieved coefficients of Zernike polynomials in Noll order [26], describing optical aberrations in the system. Figure 2(c) shows the electric fields at the pupil plane in horizontal and vertical polarizations, generated from dipoles oscillating along the x, y and z axes. These electric fields were calculated from the term $w_{mn}T_a$ defined in Eq. (4). The bright ring in each magnitude image represents the effect of SAF [Fig. 2(c)].

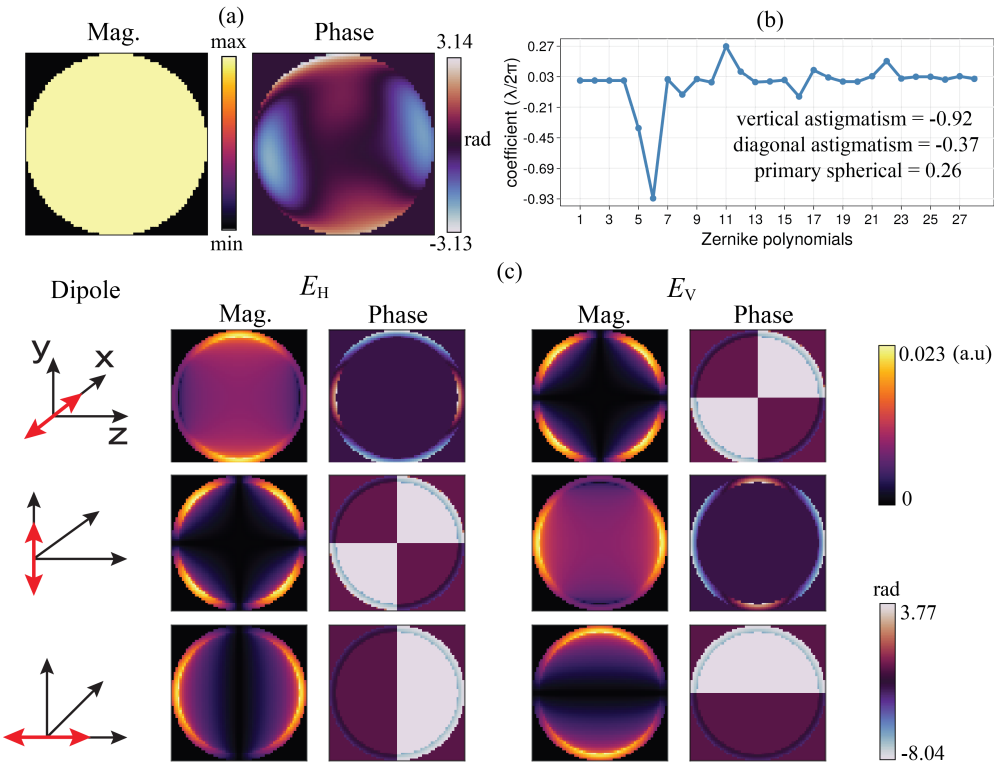

Fig. 2. **a:** Magnitude and phase of the extracted pupil function from the *in-situ* PSF modeling. **b:** Zernike coefficients of the pupil phase in **a**. **c:** Pupil magnitudes and phases of the horizontal polarization (E_H) and the vertical polarization (E_V) components from a dipole oscillating along x, y and z axes. a.u: arbitrary unit, rad: radian.

3.2. Estimation of the stage tilt

The procedure for correcting the stage tilt is as follows (Fig. 3): 1) Extract the PSF model assuming index matching based on the procedure described in section 3.1. The PSF model is based on Eq. (4), where we set $n_{\text{med}} = n_{\text{imm}}$, and z_s a value between 0.6 μm to 1 μm. In the case of index matching, the value of z_s doesn't affect the learning results. However, as $z_i \geq 0$, z_s should be large enough to ensure the effective axial position $z_i - z_s$ covers a sufficient axial range (e.g., -1 μm to 1 μm). z_s is fixed during PSF learning. 2) Perform 3D localization of the SMLM data using the obtained PSF model from step 1. The localization algorithm is based on a maximum likelihood estimator (MLE) using a spline PSF model [18,27]. 3) Due to the stage tilt, emitters at the coverslip will have different z positions, and this variation in z is relative to the immersion medium. As the PSF model from step 1 is also relative to the immersion medium, the resulting z positions of the emitters on the coverslip reflect the stage tilt. To select emitters at the coverslip, we first segment the FOV into small subregions, e.g. 6×6 subregions. We

Biomedical Optics EXPRESS

assume the stage tilt within each subregion is negligible. Second, in each subregion, we generate the histogram of emitters' z positions and identify the position of the first peak from the axial distribution. The axial position of the first peak is close to the average z position of the emitters at the coverslip. We then select the emitters with z less than the identified first-peak position and categorize them as the emitters at the coverslip. 4) For emitters at the coverslip, we assume the emitter's z position has a linear relationship with its lateral position,

$$z = \beta_1 x + \beta_2 y + \beta_3, \tag{25}$$

where $\beta_i, i = 1, 2, 3$ are unknown parameters, describing the stage tilt. Applying a least-squares estimation to solve β_i, we have

$$\hat{\beta} = (X^T X)^{-1} X^T Y. \tag{26}$$

The matrix X is constructed from the row vectors $[x_j, y_j, 1]$ with j indexing over the emitters, and the vector Y represents emitters' z positions. 5) Extract the PSF model assuming index mismatching and applying the estimated stage tilt $\hat{\beta}$. The PSF model is defined by Eq. (4), where we set $n_{\text{med}} = 1.33$ and $n_{\text{imm}} = 1.516$. The stage position of each emitter is,

$$z_s = \hat{\beta}_1 x_{\text{pixel}} + \hat{\beta}_2 y_{\text{pixel}} + z_0, \tag{27}$$

where x_{pixel} and y_{pixel} are the pixel coordinates of the emitter and are constant during PSF learning. z_0 is the stage position when the emitter's pixel coordinate is $(0, 0)$. During PSF extraction, z_0 is optimized under the constraint of $z_s \geq 0$ for all emitters. Additionally, a regularization term is applied in the loss function to minimize z_0, so that the learned axial positions z_i of the emitters on the coverslip are close to zero. 6) As the PSF learning process incorporates the stage tilt, the learned z_i for all candidate emitters should reflect the actual distances of the emitters to the coverslip. Therefore, emitters on the coverslip can be easily separated from the other emitters by the distribution of z_i. 7) Similar to step 4, the residue stage tilt $\delta\beta$ can be estimated from the selected emitters at the coverslip, where

$$z_i = \delta\beta_1 (x_{\text{pixel}} + x_i) + \delta\beta_2 (y_{\text{pixel}} + y_i) + \delta\beta_3. \tag{28}$$

Then the total residue stage tilt within the FOV is

$$\delta z_s = \max(\delta\beta_1 L_x, \delta\beta_2 L_y), \tag{29}$$

where L_x and L_y are the lateral dimensions of the FOV. 8) If the residue stage tilt δz_s>5 nm, update the stage tilt coefficients $\hat{\beta} = \hat{\beta} + \delta\beta$ and repeat from step 5. If δz_s<5 nm, output the final PSF model together with the stage tilt coefficients for localization.

3.3. Quantification of the stage tilt estimation

The estimation precision of β is related to both the emitter density at the coverslip and the degree of stage tilt. To quantify the estimation precision of β, we assume that the linear least-squares estimate $\hat{\beta}$ is the best linear unbiased estimator (BLUE). Therefore, given a finite number of samples, the variance of $\hat{\beta}$ can be estimated from [28]

$$\sigma^2_{\beta_i} = \epsilon^2 \left[(X^T X)^{-1} \right]_{ii}, \tag{30}$$

where ϵ^2 is the regression standard error and can be estimated from [28]

$$\epsilon^2 = \frac{\sum_k \sigma^2_{zk}}{n - p}. \tag{31}$$

The variance σ^2_{zk} is the variance in localizing the z position of the kth emitter on the coverslip, as detailed in step 2 of the stage tilt estimation (section 3.2). The values of σ^2_{zk} can theoretically

Biomedical Optics EXPRESS

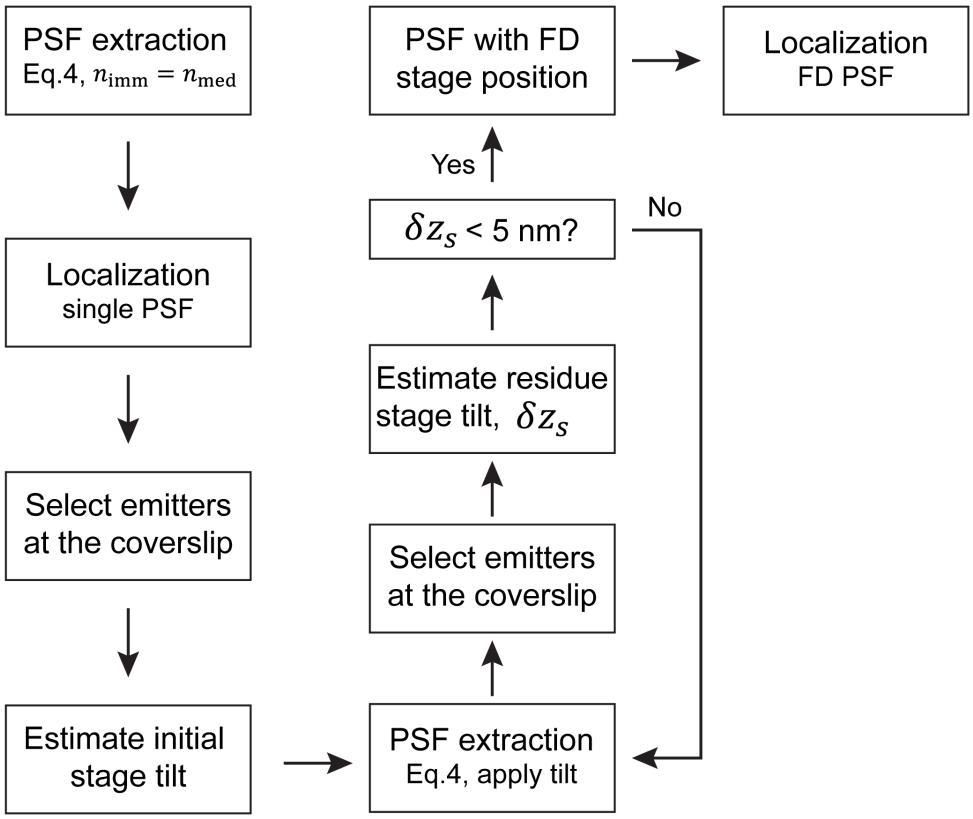

Fig. 3. Workflow for stage tilt correction. The output PSF model is used for 3D localization. FD: field-dependent. n_{imm}: refractive index of the immersion medium, n_{med}: refractive index of the sample medium. δz_s: total residue stage tilt across the field of view.

be calculated from the CRLB. n is the number of emitters on the coverslip, p is the number of estimation parameters, which is 3. As β_1 and β_2 are unitless, to quantify the estimation precision in physical units, we define the estimation precision of total stage tilt in x and y dimensions as

$$\sigma_{\Delta z_{sx}} = \sigma_{\beta_1} L_x, \tag{32}$$

$$\sigma_{\Delta z_{sy}} = \sigma_{\beta_2} L_y. \tag{33}$$

And we define the total stage tilt over the FOV as

$$\Delta z_s = \Delta z_{sx} + \Delta z_{sy} = \beta_1 L_x + \beta_2 L_y. \tag{34}$$

We found that the estimation precisions for stage tilt are below 5 nm when the emitter density is higher than 0.5 emitter per μm^2 [Fig. S1(a)]. Here, we assume that the total photons per emitter is 1000 and the background photons per pixel is 50. Given 1 emitter per μm^2, the estimation precisions decrease slightly with increasing total stage tilt [Fig. S1(b)]. Here, we assume that the maximum total stage tilt within a FOV of 30×30 μm^2 is 1 μm, where the emitters on the coverslip can still be well localized. However, with a high NA objective, a total stage tilt of 1 μm over a FOV of 30×30 μm^2 is easy to observe and shall be mechanically reduced.

After stage tilt estimation, we obtain a field-dependent PSF model spanning over the emitter's position z_i and the stage position z_s. According to Eq. (4), a given pair of (z_i, z_s) uniquely

Biomedical Optics EXPRESS

determines a 2D PSF pattern. Therefore, with an accurate estimate of the stage position z_s, the estimated emitter's position z_i shall reflect the emitter's actual distance to the coverslip. To verify the accuracy of our PSF model, we compared the PSF model with the measured emitter patterns at a set of coordinates (z_i, z_s) (Fig. S2). To incorporate the extra broadening from the single-molecule emission patterns, we rewrite Eq. (10) as

$$\mu = s \cdot (\mu_0 \otimes G) + b, \tag{35}$$

where G is a 2D Gaussian kernel, whose standard deviations in x and y dimensions are learned during the *in-situ* PSF modeling [18]. The symbol $\otimes$ denotes convolution. We partition the emitters used in stage tilt estimation into small subsets. Each subset contains emitters within a 30×30 nm^2 region in the space of (z_i, z_s). We compared the averaged emitter patterns and the corresponding emitters' models for each subset [Fig. S2(a,b)]. The models match well with the emitter patterns. We also quantified the similarity between the models and the data using a normalized mean square error,

$$NMSE = \frac{\text{avg}\left[(\mu_k - D_k)^2\right]}{\text{avg}(D_k)}, \tag{36}$$

where D represents the data, and k indexes over the pixels of each emitter pattern. Assume D_k follows the Poisson distribution, an accurate model μ_k shall result in an *NMSE* close to 1, as shown in Fig. S2(d).

3.4. Localization incorporating stage tilt

Due to the stage tilt, the PSF model varies across the FOV, a single PSF model can no longer accurately model the single-molecule emission patterns. From the process of the stage-tilt estimation described in section 3.2, we obtain the pupil function $h(k_x, k_y)$, the stage position at the pixel coordinate $(0, 0)$ z_0, and the stage tilt coefficients β_1 and β_2. With these parameters, the PSF model at any lateral position can be generated. For localization, we divide the FOV into 10×10 subregions. For each subregion, we generate the PSF model at the pixel coordinate of the subregion center and assume that the stage tilt within the subregion is negligible. The generated PSF model is a 3D matrix, with a lateral dimension of 21×21 pixels and an axial dimension of 121 slices at a step size of 2 nm. A set of spline coefficients is calculated given the generated PSF model and is used for localizing the emitters within the subregion [18,27]. By incorporating the stage tilt in localization, the estimated emitters' axial positions will reflect the actual distances of the emitters to the coverslip.

4. Results

4.1. Theoretical estimation precision

We first compared the theoretical estimation precisions of the three SAF-SMLM techniques by calculating the CRLB as described in section 2.2. The first method is single-channel SAF-PSF modeling, which is based on a single-channel imaging system that detects the single-molecule emission patterns with a camera. In this method, the fluorescence emission from the entire pupil is collected in the same channel [Fig. 4(a)]. The second method is dSALM with PSF modeling, which splits the fluorescence emission from the UAF and SAF parts of the pupil into two channels. The emission pattern from each channel is detected by a camera [Fig. 4(b)]. The third method is dSALM with photometry. This method also splits the UAF and SAF. Instead of using a camera, a point detector is used to collect all photons from each channel [Fig. 4(c)]. In photometric detection, the emitter's z position is estimated from the photon counts of both the UAF and SAF channels. For the first two detection methods, the emitter's z position is estimated

Biomedical Optics EXPRESS

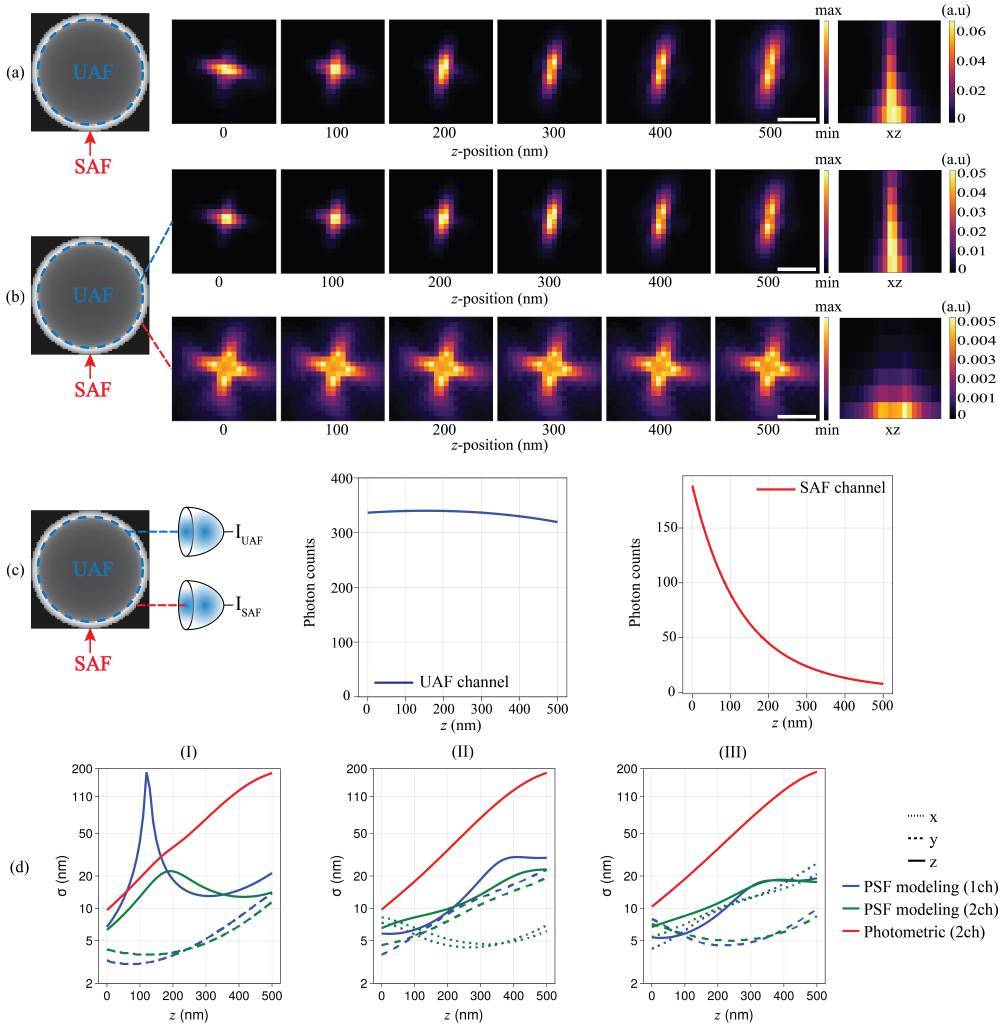

Fig. 4. **a:** Pupil and corresponding PSFs of a single-channel system with astigmatism aberration. **b:** Pupil and corresponding PSFs of a two-channel system, where UAF and SAF parts are split into two channels. The same astigmatism aberration was applied. **c:** Pupil and corresponding photon outputs of a photometric detection system. The UAF and SAF parts are split into two channels, and the photon count from each channel is detected by a point detector. The photon count from the SAF channel decays exponentially with the emitter's distance to the coverslip. **d:** Localization precision vs. emitters' z positions when using a PSF model (I) without aberration, (II) with astigmatism, and (III) from *in-situ* PSF modeling. Astigmatism improves axial precision for PSF modeling-based methods but has little effect on photometric detection.

by fitting the emission pattern with a pre-extracted PSF model [Fig. 4(a,b)]. The corresponding pupil function of the extracted PSF model is shown in Fig. 2(a,b). For CRLB calculations, the emission patterns were generated as 2D images of 21×21 pixels, with a pixel size of 129 nm. The photons detected by the photometric method are obtained by summing over the 2D images from both channels. We set the emission wavelength $\lambda = 680$ nm and the numerical aperture $n_a = 1.49$. To incorporate the index mismatch and SAF, we set the refractive indices of the sample medium $n_{\text{med}} = 1.33$ and the immersion medium $n_{\text{imm}} = 1.516$. The photon count of

Biomedical Optics EXPRESS

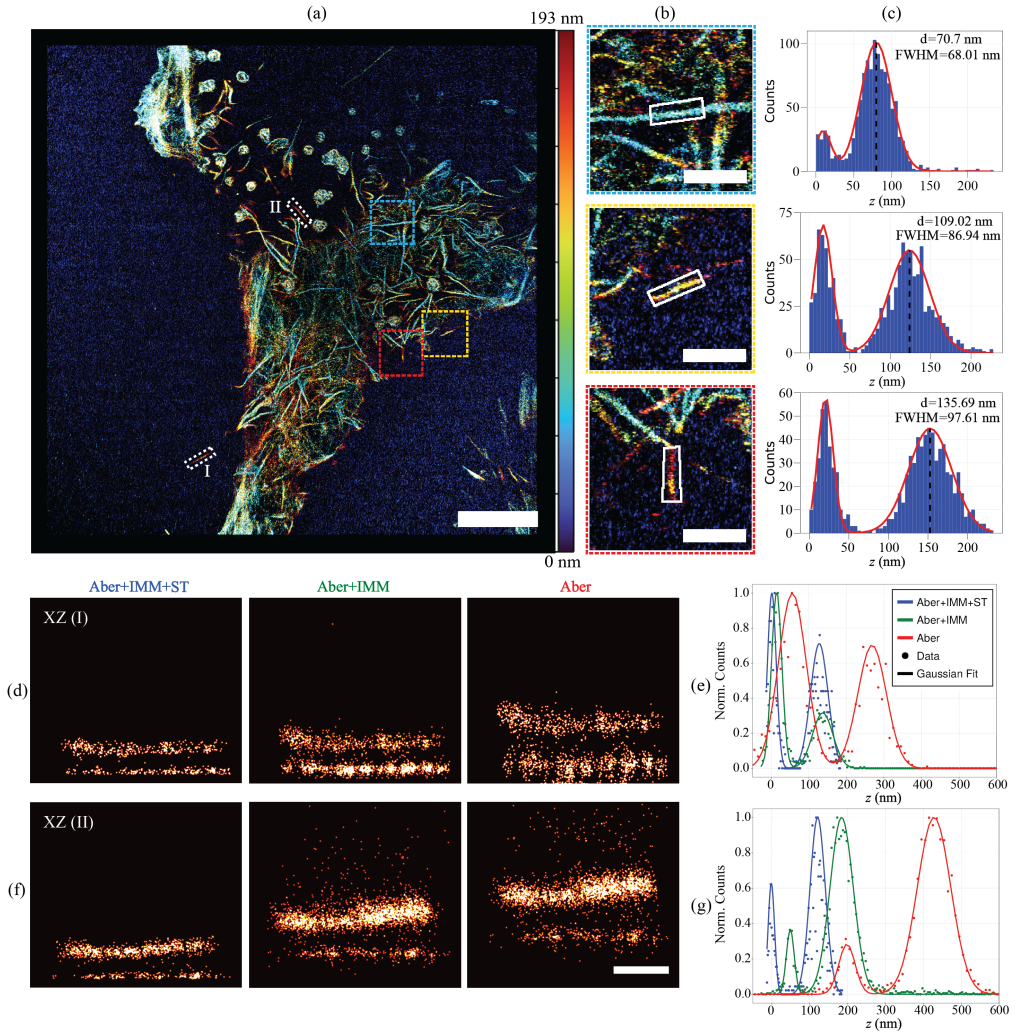

Fig. 5. a: Three-dimensional reconstruction of F-actin in HeLa cells. Color is scaled with emitters' z positions. **b:** Zoomed-in images of selected regions in **a**, indicated by the cyan, yellow, and red boxes. **c:** Histograms of emitters' z positions in selected regions (white boxes) in **b**. Each histogram was fitted by a two-Gaussian model (red line). The first peak indicates the emitters on the coverslip. The full width at half maximum (FWHM) of the second peak quantifies the axial resolution of the actin. The FWHM increases as the actin's distance (d) to the coverslip increases. **d:** XZ view of region I in **a**, reconstructed from three different PSF modeling methods: Aber+IMM+ST, Aber+IMM, and Aber. In the two-line structure, the lower line indicates the emitters at the coverslip, and the upper line indicates the actin filament. **e:** Histogram of z localizations in **d**. Color represents different PSF modeling methods. Each histogram (dots) was fitted by a two-Gaussian model (solid line). **f-g:** Same as **d** and **e**, for region II in **a**. For Aber and Aber+IMM, the axial position of the coverslip changes at different regions of the FOV (regions I and II in **a**). With stage tilt correction, the Aber+IMM+ST method reduces the lateral dependency of the coverslip's axial position. Scale bars 5 μm (**a**), 1 μm (**b**), and 300 nm (**f**).

Biomedical Optics EXPRESS

each emitter is 5000. The background photon per pixel for the single-channel system is 40, and for the UAF and SAF channels is 35 and 5, respectively. As the SAF takes only a small part of the pupil, the background from the SAF channel is also small.

First, we compared the theoretical precisions of the three SAF-SMLM methods under the ideal condition with no aberration [Fig. 4(d,I)]. Both PSF-modeling based methods show a peak in the axial precision at z around 100-200 nm, which is close to the focal plane where the lateral precision is the highest. The focal plane position is related to the stage position z_s, here, we set z_s to 183 nm. Next, we added a vertical astigmatism of -1 $\lambda/2\pi$ to the pupil function [Fig. 4(d,II)]. The magnitude of the aberration quantifies the root mean square error (RMS) of the wavefront. We found that astigmatism effectively improves the axial precision for PSF-modeling based methods, but has minimal effect on the photometric method. Furthermore, single-channel SAF-PSF modeling achieves the best axial precision when emitters are within 200 nm of the coverslip. Separating the UAF and SAF into two channels (dSALM with PSF modeling) slightly lower the precision, which could be caused by the loss of information when the fluorescence emission from the UAF and SAF is not added coherently. The photometric method results in the lowest axial precision, as the summation of all pixels within a 2D image ignores all information from the PSF patterns. Lastly, we compared the precision under a realistic condition, where an *in-situ* PSF model extracted from an SMLM dataset is used [Fig. 4(d,III)]. We found that single-channel SAF-PSF modeling outperforms the other two methods in axial precision when the emitter's distance to the coverslip is less than 300 nm. The *in-situ* PSF model contains a spherical aberration of 0.26 $\lambda/2\pi$ [Fig. 2(a,b)], which further improves the axial precision of the single-channel method (Fig. S3). The lateral precisions of both PSF-modeling methods are similar for all conditions. The photometric method alone cannot estimate the emitter's lateral position. It is often combined with a two-channel system for 3D localization (see section 2.2). Therefore, in Fig. 4(d), the lateral precision of the photometric method is not shown.

We further investigated the effect of stage positions and aberrations on axial precision for the three SAF-SMLM methods (Fig. S3). We found that increasing stage position and adding astigmatism will both improve the axial precision of single-channel SAF-PSF modeling. And a small positive spherical aberration further improves its precision, especially at lower stage positions. We next examined the axial precision of those imaging methods at different background levels (Fig. S4). We found that dSALM-based methods are sensitive to the background level in the SAF channel. With zero background in the SAF channel, for localizing emitters close to the coverslip, dSALM with PSF modeling slightly outperforms the single-channel method at high background levels in the UAF channel; we also found that the performance of both dSALM based methods becomes similar at high UAF background levels. However, with a more practical background level in the SAF channel, such as 5 photons per pixel, the single-channel method performs the best when localizing near coverslip emitters; and the precision of the photometric method reduces dramatically.

4.2. Reconstruction of the actin filament

We next compared different PSF modeling methods on astigmatism imaging of F-actin in HeLa cells labeled with lifeact-Atto 655. The first PSF modeling method considers only the systematic aberrations from the imaging system and assumes the refractive index of the sample medium matches that of the immersion medium, termed Aber. The second method considers both the systematic aberrations and the index mismatch aberration, termed Aber+IMM. Both methods assume the PSF model is spatially invariant across the FOV. The third method incorporates both the systematic and index mismatch aberrations, as well as the stage tilt in the PSF model, termed Aber+IMM+ST. This method generates a field-dependent PSF model as described in section 3.4. Figure 5(a-c) shows the reconstruction of the actin filament from Aber+IMM+ST. We selected three actin filaments at different axial positions [Fig. 5(b)] and plotted the histogram

Biomedical Optics EXPRESS

of the estimated emitters' z positions in each selected region [Fig. 5(c)]. The histograms show a two-peak distribution. The first peak is from emitters at the coverslip due to the non-specific binding of the fluorescent tag to the coverslip. The second peak is from emitters at the actin filament. By fitting the histogram with a two-Gaussian model, we found the distances of the actin filaments to the coverslip are 70.7 nm, 109.02 nm and 135.69 nm, and the widths of the actin filaments along the z dimension are 68.01 nm, 86.94 nm and 97.61 nm, respectively. As expected, the axial width of the filament increases with its distance to the coverslip, indicating a decrease in axial resolution. We also found that the axial positions of the first peak in the histograms are located at 9.49 nm, 16.92 nm, and 20.28 nm, respectively. Ideally, the axial distribution of the emitters at the coverslip should peak at $z = 0$ nm. However, due to residue stage tilt and bias in estimating the stage position at lateral coordinate $(0, 0)$, z_0, there is an offset of 10-20 nm to the estimated z positions of the emitters at the coverslip. For comparison of the three PSF modeling methods, we selected two actin filaments at well-separated lateral positions [Fig. 5(d,f)]. We aligned the coordinates from the three methods in both lateral and axial dimensions. For axial alignment, we selected the coordinates of each method from the lower right corner of the FOV, and estimated the peak position of the axial distribution through a Gaussian fitting. Then the z coordinates of each method were subtracted from the estimated peak position, so that the z coordinates of the three methods are aligned at the lower right corner of the FOV. Without correcting the stage tilt, both Aber and Aber+IMM show a larger lateral dependency of the coverslip's axial position, indicated by the bottom lines in Fig. 5(d,f) and first peaks in Fig. 5(e,g). Additionally, due to inaccurate PSF models, Aber and Aber+IMM also result in a larger axial spread for emitters both at the coverslip and filaments, indicating lower axial resolution. Aber performs the worst due to the larger deviation of the PSF model from true single-molecule emission patterns. The estimated stage positions at regions I and II are 290 nm and 140 nm, respectively [Fig. 5(a) and Fig. S5]. At a larger stage position, the coverslip is farther away from the focal plane. For an index-matched PSF model (Aber), the axial precision near the coverslip is lower (Fig. S6), leading to a larger axial spread of emitters at the coverslip in region I [Fig. 5(d-g)]. By incorporating the stage tilt, Aber+IMM+ST shows consistent coverslip positions at different lateral locations and the smallest axial spread of emitters at different z positions.

5. Methods

5.1. Sample preparation

HeLa cells were originally purchased from American type culture collection (ATTC). The short-tandem repeat analysis was performed to authenticate the HeLa cells. The cell culture was done in Dulbecco's Modified Eagle Medium and kept in an incubator that was set at 37°C and at 5% carbon dioxide level. Cells were plated overnight on a 25 mm round coverslip for imaging. On the following day, cells were fixed using a cytoskeleton-preserving buffer which contained 80 mM Pipes, 5 mM EGTA, and 2 mM $MgCl_2$ (PEM) at pH 7.2. Cells were briefly washed with warm PEM before a two-step fixation. In the first step, cells were fixed for 60 seconds in 0.6% paraformaldehyde (PFA) with 0.1% glutaraldehyde (GA) and 0.25% Triton diluted in PEM buffer. In the second step, cells were fixed for 2 hours in 4% PFA and 0.2% GA diluted in PEM buffer followed by a 2x wash with phosphate buffered saline (PBS). To quench the background fluorescence of GA, cells were incubated in 0.1% $NaBH_4$ for 10 minutes followed by a 2x wash with PBS. Cells were incubated in 10 mM Tris for 10 minutes to suppress reactive cross-linkers followed by a 2x wash with PBS. Cells were permeabilized by incubating for 15 mins in 5% bovine serum albumin (BSA) and 0.05% Triton X-100 diluted in PBS. Finally, cells were washed once in PBS before proceeding for the labeling process. To label cells, we used 17-amino acid peptide "lifeact" conjugated to Atto 655 (sequence: [Atto 655] CMGVADLIKKFESISKEE[COOH] (Bio-Synthesis, Lot No. P5869-1)). The imaging buffer consists of 10 mM HEPES, 150 mM

Biomedical Optics EXPRESS

NaCl, 10% glucose, and 0.1% BSA with an adjusted pH of 7.0. The lifeact was diluted to 0.26 nM in the imaging buffer. The 25 mm coverslip with cells plated on it was placed into an Attofluor cell chamber (Life Technologies, Cat No. A-7816) following the addition of imaging buffer into the chamber. A clean coverslip was placed to seal the chamber to avoid a change in buffer pH due to oxygen permeation.

5.2. Data acquisition

The samples were mounted on the microscope stage using a custom designed chamber holder. The microscope setup was constructed using a commercially available inverted microscope (IX71, Olympus America Inc.). A nano-positioning stage (Mad City Labs, Nano-Drive MCLC02135) was set up on the microscope for cell location and brightfield registration. A lamp (Olympus U-LH100 L-3) mounted on the microscope was used to collect images for brightfield registration [29]. The cell sample was excited using a 642 nm diode laser (Thorlabs HL6366DG), with the laser light coupled into a single-mode optical fiber (Thorlabs P1-488PM-FC-1). The laser beam was collimated using a collimating objective (Olympus Plan N, 40x 0.1 NA). The collimated laser beam was reflected from a quad-edge laser dichroic beamsplitter (Semrock 405/488/561/635) and focused onto the back focal plane (BFP) of an oil immersion TIRF objective lens (Olympus UApo N, 100x 1.49 NA). The emitted fluorescence from the sample was then transmitted through a quad-band bandpass emission filter (Semrock 446/523/600/677). A 4f relay system consisting of two lenses of focal lengths of 150 mm and 125 mm was set up in the emission path. At the Fourier plane, we have set up two cylindrical lenses of focal lengths of 1 m and -1 m respectively, for introducing astigmatism. The emitted fluorescence was collected through a bandpass filter (Semrock FF02-685/40-25) on a sCMOS camera (Hamamatsu ORCA Flash 4.0 C11440). The camera exposure time for actin imaging was set to 40 ms for lifeact imaging [30]. Bright-field registration was utilized to correct sample drift after every 2000 frames. All the instruments attached to the microscope were controlled using custom-written software in MATLAB (MathWorks Inc.) [31]. The SMLM setup is highly sensitive to sample drift along the axial direction due to its extended data acquisition duration, ranging from tens of minutes to hours. This axial drift needs to be compensated before starting to collect the fluorescence imaging data [29]. For this, bright-field images of the sample along the axial direction were recorded as a reference image stack. During the collection of fluorescence imaging data, bright-field images of the sample were collected after every acquisition cycle (2000 frames). Then similarities of these images were compared with the reference images and their 2D correlation was calculated which was subsequently fitted to find the image that is most similar to the reference image. Then z position of this image is considered the best in-focus position for the next round of data collection.

5.3. Data analysis

A custom-written package in Julia, SMLMVis, was used for rendering the super-resolution images. The PSF models were extracted using the uiPSF package [18]. Localizations of the actin filaments using a single PSF model (Aber and Aber+IMM methods) were performed on SMAP [32]. The localization of the actin filaments using the stage-tilt corrected PSF model (Aber+IMM+ST method) was performed on a custom-written algorithm in Python.

6. Conclusion and discussion

In summary, we introduced a single-channel SAF-PSF modeling method for SAF-SMLM imaging. We demonstrated that a single-channel system with astigmatism aberration can effectively exploit the information from SAF. Separation of the UAF and SAF into two channels will cause information loss. The commonly used photometric detection by summing over the emission pattern further reduces the information. However, PSF-modeling based method is more sensitive

Biomedical Optics EXPRESS

to stage tilt. We introduced a stage-tilt correction algorithm to enable accurate and precise localization using a single-channel system.

Our stage-tilt correction algorithm requires a sufficient number of emitters on the coverslip, ideally covering the entire FOV. We found that an emitter density higher than 0.5 emitter per μm^2 shall achieve the required precision for stage tilt estimation (Fig. S1). This condition can often be met by non-specific binding of the fluorescent labels to the coverslip. For the stage-tilt estimation from the presented actin data, the emitter density at the coverslip is 1 emitter per μm^2 (Fig. S2). We expect that our stage-tilt correction algorithm can also benefit other 3D imaging techniques in the presence of SAF. Furthermore, our stage-tilt correction algorithm assumes a planar tilt over the FOV. For a small FOV in our application and assuming no bending of the coverslip, a planar tilt approximation is sufficient. However, for a larger FOV, field curvature needs to be considered, which will make the effective stage tilt curved. In addition, field-dependent aberration should also be incorporated. Our stage tilt correction method can be further extended to a large FOV. Briefly, the *in-situ* PSF modeling steps in Fig. (3) shall be modified to extract field-dependent aberrations (without defocus), and the z positions of the emitters on the coverslip could be modeled by higher-order models, such as the Legendre polynomials [33].

Our single-channel SAF-PSF modeling method is based on astigmatism imaging. Zelger et al. demonstrated that the bi-plane method outperforms the astigmatism method in exploiting the information of SAF [17]. However, their demonstrations lack comparisons with other PSF engineering techniques, such as the double-helix PSF [9]. We demonstrated that astigmatism plus a small positive spherical aberration further improves the precision (Fig. S3). Therefore, the optimal 3D imaging technique that fully exploits the information of SAF requires further investigation.

In conclusion, our findings indicate that a single-channel system with astigmatism is sufficient to achieve the resolution enhancement provided by SAF. A complex system separating UAF and SAF into two channels is not required. We recognized that a recent work utilizing both the z-dependent excitation intensity from TIRF illumination and SAF achieves high axial resolution using a single-channel system [34]. However, this method requires TIRF illumination and calibration of the z-dependent excitation intensity. Our method is independent of excitation and requires no z-dependent intensity calibrations [12,35], which can be affected by various factors, such as blinking and non-uniform illumination [34]. We believe that our method will make SAF-SMLM more accessible for a wide range of applications in biological sciences.

Funding. National Institutes of Health (1R01GM140284); National Science Foundation (2039517); U.S. Department of State Fulbright scholarship; Zancada Graduate Fellowship Program from the UNM Office of the Vice President for Research (OVPR).

Disclosures. The authors declare no conflict of interest.

Data availability. Raw SMLM data of the actin filaments are available upon request.
Code availability. The source codes used in this work are available upon request.

Supplemental document. See Supplement 1 for supporting content.

References

1. E. Betzig, G. H. Patterson, R. Sougrat, *et al.*, "Imaging intracellular fluorescent proteins at nanometer resolution," Science **313**(5793), 1642–1645 (2006).
2. S. T. Hess, T. P. Girirajan, and M. D. Mason, "Ultra-high resolution imaging by fluorescence photoactivation localization microscopy," Biophys. J. **91**(11), 4258–4272 (2006).
3. M. J. Rust, M. Bates, and X. Zhuang, "Sub-diffraction-limit imaging by stochastic optical reconstruction microscopy (storm)," Nat. Methods **3**(10), 793–796 (2006).
4. B. Huang, W. Wang, M. Bates, *et al.*, "Three-dimensional super-resolution imaging by stochastic optical reconstruction microscopy," Science **319**(5864), 810–813 (2008).
5. P. Prabhat, S. Ram, E. S. Ward, *et al.*, "Simultaneous imaging of different focal planes in fluorescence microscopy for the study of cellular dynamics in three dimensions," IEEE Trans.on Nanobioscience **3**(4), 237–242 (2004).
6. M. F. Juette, T. J. Gould, M. D. Lessard, *et al.*, "Three-dimensional sub–100 nm resolution fluorescence microscopy of thick samples," Nat. Methods **5**(6), 527–529 (2008).

Biomedical Optics EXPRESS

7. G. Shtengel, J. A. Galbraith, C. G. Galbraith, *et al.*, "Interferometric fluorescent super-resolution microscopy resolves 3d cellular ultrastructure," Proc. Natl. Acad. Sci. **106**(9), 3125–3130 (2009).
8. S. Prasad, "Rotating point spread function via pupil-phase engineering," Opt. Lett. **38**(4), 585–587 (2013).
9. M. P. Backlund, M. D. Lew, A. S. Backer, *et al.*, "The double-helix point spread function enables precise and accurate measurement of 3D single-molecule localization and orientation," Proceedings of SPIE–the International Society for Optical Engineering **8590**, 85900L (2013).
10. Y. Shechtman, S. J. Sahl, A. S. Backer, *et al.*, "Optimal point spread function design for 3d imaging," Phys. Rev. Lett. **113**(13), 133902 (2014).
11. A. Aristov, B. Lelandais, E. Rensen, *et al.*, "Zola-3d allows flexible 3d localization microscopy over an adjustable axial range," Nat. Commun. **9**(1), 2409 (2018).
12. N. Bourg, C. Mayet, G. Dupuis, *et al.*, "Direct optical nanoscopy with axially localized detection," Nat. Photonics **9**(9), 587–593 (2015).
13. J. Deschamps, M. Mund, and J. Ries, "3d superresolution microscopy by supercritical angle detection," Opt. Express **22**(23), 29081–29091 (2014).
14. A. Dasgupta, J. Deschamps, U. Matti, *et al.*, "Direct supercritical angle localization microscopy for nanometer 3d superresolution," Nat. Commun. **12**(1), 1180 (2021).
15. C. Cabriel, N. Bourg, P. Jouchet, *et al.*, "Combining 3D single molecule localization strategies for reproducible bioimaging," Nat. Commun. **10**(1), 1980 (2019).
16. P. Zelger, L. Bodner, L. Velas, *et al.*, "Defocused imaging exploits supercritical-angle fluorescence emission for precise axial single molecule localization microscopy," Biomed. Opt. Express **11**(2), 775 (2020).
17. P. Zelger, L. Bodner, M. Offterdinger, *et al.*, "Three-dimensional single molecule localization close to the coverslip: a comparison of methods exploiting supercritical angle fluorescence," Biomed. Opt. Express **12**(2), 802 (2021).
18. S. Liu, J. Chen, J. Hellgoth, *et al.*, "Universal inverse modeling of point spread functions for SMLM localization and microscope characterization," Nat. Methods **21**(6), 1082–1093 (2024).
19. M. Lelek, M. T. Gyparaki, G. Beliu, *et al.*, "Single-molecule localization microscopy," Nat. Rev. Methods Primers **1**(1), 39 (2021).
20. S. Liu, S. Pani, S. A. Khan, *et al.*, "Separation measurement of two freely rotating dipole emitters at near optimal precision," bioRxiv (2025).
21. S. Liu, E. B. Kromann, W. D. Krueger, *et al.*, "Three dimensional single molecule localization using a phase retrieved pupil function," Opt. Express **21**(24), 29462 (2013).
22. Y. Li, Y.-L. Wu, P. Hoess, *et al.*, "Depth-dependent psf calibration and aberration correction for 3d single-molecule localization," Biomed. Opt. Express **10**(6), 2708–2718 (2019).
23. S. M. Kay and J. Love, *Fundamentals of Statistical Signal Processing: Estimation Theory* (Prentice Hall, 1993).
24. R. J. Ober, S. Ram, and E. S. Ward, "Localization accuracy in single-molecule microscopy," Biophys. J. **86**(2), 1185–1200 (2004).
25. P. Zhang, S. Liu, A. Chaurasia, *et al.*, "Analyzing complex single-molecule emission patterns with deep learning," Nat. Methods **15**(11), 913–916 (2018).
26. R. J. Noll, "Zernike polynomials and atmospheric turbulence," J. Opt. Soc. Am. **66**(3), 207 (1976).
27. Y. Li, M. Mund, P. Hoess, *et al.*, "Real-time 3d single-molecule localization using experimental point spread functions," Nat. Methods **15**(5), 367–369 (2018).
28. F. Hayashi, *Econometrics* (Princeton University Press, Princeton, 2011).
29. M. J. Wester, D. J. Schodt, H. Mazloom-Farsibaf, *et al.*, "Robust, fiducial-free drift correction for super-resolution imaging," Sci. Rep. **11**(1), 23672 (2021).
30. H. Mazloom-Farsibaf, F. Farzam, M. Fazel, *et al.*, "Comparing lifeact and phalloidin for super-resolution imaging of actin in fixed cells," PLoS One **16**(1), e0246138 (2021).
31. S. A. Khan, S. Pallikkuth, D. J. Schodt, *et al.*, "A matlab-based instrument control (mic) package for fluorescence imaging," Journal of Open Source Software **10**(105), 7275 (2025).
32. J. Ries, "Smap: a modular super-resolution microscopy analysis platform for smlm data," Nat. Methods **17**(9), 870–872 (2020).
33. I. Droste, E. Schuitema, S. Khan, *et al.*, "Calibration-free estimation of field dependent aberrations for single molecule localization microscopy across large fields of view," Optica, accepted for publication 2025, 10.1364/OPTICA.560721.
34. A. M. Szalai, B. Siarry, J. Lukin, *et al.*, "Three-dimensional total-internal reflection fluorescence nanoscopy with nanometric axial resolution by photometric localization of single molecules," Nat. Commun. **12**(1), 517 (2021).
35. C. Cabriel, N. Bourg, G. Dupuis, *et al.*, "Aberration-accounting calibration for 3D single-molecule localization microscopy," Opt. Lett. **43**(2), 174 (2018).